Hypothetical Cirrus Band Generation for Advanced Himawari Imager Sensor Using Data-to-Data Translation With Advanced Meteorological Imager Observations

Jeong-Eun Park, Yun-Jeong Choi, Jaehoon Jeong, and Sungwook Hong

***Abstract*—Cirrus cloud contributes significantly to earth's radiation budget and the greenhouse effect. The Advanced Himawari Imager (AHI) onboard the Himawari-8 satellite lacks a 1.37 μm band, sensitive to monitoring cirrus clouds. This article proposed a conditional generative adversarial network-based data-to-data translation (D2D) model to generate a hypothetical AHI 1.37 μm band. For training and testing the D2D model, the Geo-Kompsat-2A Advanced Meteorological Imager (AMI) 1.37 μm bands and other highly correlated bands to cirrus from July 24, 2019 to July 31, 2020, were used. The D2D model exhibited a high level of agreement (mean of statistics: correlation coefficient (CC) = 0.9827, bias = 0.0004, and root-mean-square error (RMSE) = 0.0086 in albedo units) between the observed and D2D-generated AMI 1.37 μm bands from validation datasets. The application of the D2D model to the AHI sensor showed that the D2D-generated AHI 1.37 μm band was qualitatively analogous to the observed AMI 1.37 μm band (average of statistics: bias = 0.0026, RMSE = 0.0191 in albedo units, and CC = 0.9158) on the 1st, 15th, and 28th of each month of 2020 in the common observing regions between Korea and Japan. The validation results with the CALIPSO data also showed that the D2D-generated AHI 1.37 μm band performed similarly to the observed AMI 1.37 μm band. Consequently, this article can significantly contribute to cirrus detection and its application to climatology.**

***Index Terms*—1.37 μm, CGAN, cirrus, data-to-data translation, geo-kompsat-2A, Himawari, satellite remote sensing.**

Manuscript received 27 August 2022; revised 15 October 2022 and 2 November 2022; accepted 22 November 2022. Date of publication 28 November 2022; date of current version 15 December 2022. This work was supported in part by the National Institute of Environment Research (NIER), Ministry of Environment (MOE), Republic of Korea, under Grant NIER-2021-01-01-052 and Grant NIER-2022-01-02-096, and in part by the Korea Meteorological Administration Research and Development Program under Grant KMI2020-00510, "Developing Service Platform Technology for AI and Data Convergence" under Grant KMA2021-00122, and Development of AI techniques for Weather Forecasting under Grant KMA2021-00121. *(Corresponding author: Sungwook Hong.)*

Jeong-Eun Park and Yun-Jeong Choi are with the Department of Environment and Energy, Sejong University, Seoul 05006, South Korea (e-mail: wjd196@sju.ac.kr; choiyunj0316@sju.ac.kr).

Jaehoon Jeong is with the National Institute of Environmental Research, Incheon 404170, South Korea (e-mail: jaehoon80@korea.kr).

Sungwook Hong is with the Department of Environment, Energy, and Geoinformatics, Sejong University, Seoul 05006, South Korea, and also with the DeepThoTh Co., Ltd., Seoul 05006, South Korea (e-mail: sesttiya@gmail.com).

Digital Object Identifier 10.1109/JSTARS.2022.3224911

I. Introduction

Cirrus cloud profoundly influences the radiation budget of the earth–atmosphere system and amplifies the greenhouse effect [1], [2], [3] because of its relatively low albedo, high altitude, and low emission temperature. Cirrus clouds contain a significant amount of large and nonspherical ice crystals, which are widely distributed throughout and affect the relative strength of the solar albedo and infrared (IR) greenhouse effects. Previous studies reported that cirrus clouds occur with a global average frequency of approximately 27% or 16.7%, and 45% or 70% for north and south tropical zones, respectively [4], [5], [6]. Cirrus clouds in the high atmosphere significantly control the global radiation budget and terrestrial thermal balance in the atmosphere owing to their constituent ice crystals and global coverage [7], [8], [9], [10].

There have been several efforts to detect cirrus using satellite remote sensing [11], [12], [13], [14], [15], [16], [17], [18], [19], [20], [21]. Specifically, the 1.37 μm band in a strong water vapor absorption spectral region has been used to detect daytime cirrus clouds [12], [14], [18] owing to its high sensitivity to thin cirrus as well as no sensitivity to the lower troposphere. However, the 1.37 μm band loses some of its advantages because of surface reflectance effect under dry atmospheric conditions (total precipitable water $<$ approximately 10 mm) [22], [23].

In satellite remote sensing, the Moderate Resolution Imaging Spectroradiometer (MODIS) [24], [25] onboard the Earth Observing System Terra and Aqua satellites, Multiangle Imaging Spectro-Radiometer onboard the Terra satellite [26], [27], Visible Infrared Imaging Radiometer Suite (VIIRS) [28], [29] onboard the Suomi National Polar-orbiting Partnership and NOAA-20 weather satellites, Landsat 8 Operational Land Imager (OLI) [30], and Sentinel-2 multispectral instrument (MSI) [31] have been employed for thin cirrus detection using 1.37 μm band.

Moreover, several next-generation meteorological geostationary satellites have been launched and operated successfully. The Himawari-8/-9 [32] with Advanced Himawari Imager (AHI) sensor, Geostationary Operational Environmental Satellite (GOES)-R [33] with Advanced Baseline Imager (ABI) sensor [34], [35], and Geokopmsat-2A (GK-2A) with Advanced Meteorological Imager (AMI) sensor [36] have 16 spectral bands

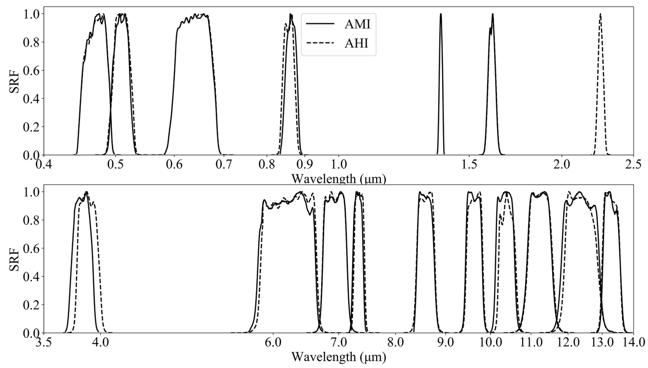

Fig. 1. Spectral responses of the AMI and AHI sensors. The dotted and solid curves represent the Himawari/AHI and GK-2A/AMI bands.

with spatial resolutions ranging from 0.5 to 2 km depending on the band, and full disk imaging from 10 to 15 min [37]. The GOES-R/ABI and GK-2A/AMI sensors have the 1.37 μm band for detecting daytime cirrus clouds, whereas Himawari-8/AHI does not have a 1.37 μm band. Therefore, the Japan Aerospace Exploration Agency (JAXA) provides the official ice cloud and surface radiation products using Himawari-8 and Global Change Observation Mission-C satellites [38], [39], [40].

The objective of this article was to produce a virtual Himawari/AHI 1.37 μm band using a data-to-data translation (D2D) with a deep-learning technique, which is an effective technique that can accurately extract suitable characteristics from satellite data. Owing to this advantage offered by deep-learning techniques, recent studies on IR [41], Synthetic Aperture Radar [42], and other types of imagery [43], [44], [45], [46] have used deep-learning techniques, including artificial neural network [47], convolutional neural network [48], and conditional generative adversarial network (CGAN) [49], [50], [51], [52], [53], [54], [55], [56].

This article proposes a D2D model that employs the CGAN technique to generate the missing Himawari-8/AHI 1.37 μm band by pairing the 1.37 μm band with other bands. The generation of the missing Himawari-8/AHI 1.37 μm band was evaluated as an adversarial problem solved by CGAN rather than other deep-learning techniques in support of training and validation for the D2D model. The D2D-generated Himawari AHI 1.37 μm band can complement the Himawari AHI for cirrus detection, cloud mask improvement, and climate studies.

II. Data

A. Satellite Data and Study Area

The AMI and AHI sensors constructed by the Harris Corporation have similar spectral responses to the visible (VIS) and IR bands. However, the AHI and AMI are missing NIR bands of 1.37 and 2.26 μm, respectively. Generally, the 1.37 and 2.26 μm bands can effectively detect cirrus clouds and ice particles in clouds, respectively. Additionally, the two sensors have similar spectral, spatial, and temporal resolutions except for the respective missing NIR band. Thus, similar amounts of energy are recorded by the AMI and AHI sensors. Notably, AHI and AMI conducted observations at 128° E and 140.7° E, respectively. Fig. 1 illustrates the spectral response functions (SRF) of AMI and AHI sensors; the dotted and solid lines represent the Himawari/AHI and GK-2A/AMI wavelength bands, respectively. Table I provides a summary of AMI and AHI sensor characteristics.

TABLE I
SPECTRAL BAND CHARACTERISTICS OF GK-2A AMI AND HIMAWARI/AHI FROM VIS TO IR BANDS

Band Number	AMI	AHI	Spatial Resolution (km)
	Central Wavelength (μm)		
1	0.47	0.46	1.0
2	0.51	0.51	1.0
3	0.64	0.65	0.5
4	0.86	0.86	2.0
5	1.37	1.61	2.0
6	1.61	2.26	2.0
7	3.83	3.85	2.0
8	6.21	6.25	2.0
9	6.94	6.95	2.0
10	7.33	7.35	2.0
11	8.59	8.60	2.0
12	9.62	9.63	2.0
13	10.35	10.45	2.0
14	11.23	11.20	2.0
15	12.36	12.35	2.0
16	13.29	13.30	2.0

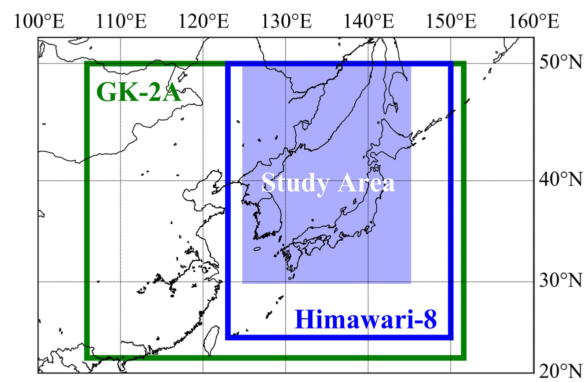

Fig. 2. Study areas with AMI extended local area and AHI Japan area.

This article chose the Far East region, encompassing the Korean Peninsula, Japan, and a portion of China between 30° and 50° N latitude, and 125° and 145° E longitude, as the study area because of the overlap between the AMI Extended Local Area and AHI Japan Area, as shown in Fig. 2.

This article used the full disk level 1 (L1B) data in the 1.37 μm and other bands of GK-2A/AMI and Himawari/AHI in 1024 × 1024 pixel-size to obtain the D2D-generated AHI 1.37 μm band data. We obtained the AMI and AHI data from the National Meteorological Satellite Center (NMSC) of the Korea Meteorological Administration (KMA) and JAXA.

B. Preprocess of Datasets

The observed GK-2A/AMI and Himawari/AHI L1B albedo and brightness temperature (TB) data were cropped into the study area by 1024 × 1024, to conserve the original data information and provide input datasets for obtaining the D2D model-generated AHI 1.37 μm bands data for training, testing, and application. The original AMI file constituted full disk data of specifications 22 000 × 22 000 (AMI red band), 11 000 × 11 000 (other VIS bands), or 5500 × 5500 (other bands); the original AHI file was gridded data with 6001 × 6001 (2 km). The AMI data were downscaled to 5500 × 5500 (2 km) using the bilinear interpolation method [57].

The proposed D2D model was trained and tested using the directly-normalized albedo and TB of the AMI and AHI observations ranging from -1 to 1, which is different from the image-to-image translation used in the Pix2Pix model.

C. CALIPSO Dataset for Validation

The Cloud Aerosol Lidar and Infrared Pathfinder Satellite Observations (CALIPSO) observe the global distribution of clouds and aerosols in earth's atmosphere. This article used the CALIPSO Level 2 lidar vertical feature mask (VFM) data products providing vertical and horizontal distribution information on cloud and aerosol layers [58]. The cloud types in the CALIPSO VFM data were classified into nine flags according to the International Satellite Cloud Climatology Project's standard definitions for meteorological cloud types [8]. The AMI, AHI, and CALIPSO data were collocated. The D2D-generated AHI 1.37 data were compared with the observed AMI 1.37 data and validated using CALIPSO VFM data with cirrus flags. The MODIS-derived threshold of 0.007 for cirrus detection [59] was applied to AMI and AHI data to determine cirrus pixels.

III. Methods

A. CGAN in D2D Model

To develop the D2D model, we used the CGAN method [49], [50]. CGAN evolved from GAN [60] and deep convolutional GAN [61], [62]. CGAN techniques have been successfully applied in a variety of image processing applications.

The D2D translation was implemented using the Pix2Pix [50], [63] as it does not include noise for G. Moreover, Pix2Pix has advantages in using U-Net [64] to create $G(X)$ for the generator, and Patch-GAN [50] for the discriminator.

Mathematically, the D2D model learns a mapping function G to obtain a virtual output dataset (Y_{D2D}) using a dataset of real input data (X) different from other GAN using a random noise vector (Z) as follows [49]:

$$G : (x_i, y_i) \in X \times Y \rightarrow y_{i,\mathrm{D2D}} \in Y_{\mathrm{D2D}} = G(X, Y) \quad (1)$$

where X and Y are the datasets of the real-observed data x_i and y_i. Y_{D2D} denotes the dataset of the D2D-generated output data $y_{j,\mathrm{D2D}}$ generated from G. The subscripts i denotes the number of input and output data.

Additionally, the data-scaling function, with D as the discriminator, is obtained as follows [49]:

$$D : P(Y_{\mathrm{D2D}} | Y) \rightarrow [0, 1] \quad (2)$$

where $P(Y_{\mathrm{D2D}}|Y)$ denotes the conditional probability ranging from 0 to 1 between the observed output (Y) and the generated output ($P(Y_{\mathrm{D2D}})$. $P(Y_{\mathrm{D2D}}|Y) = 1$ when $Y_{\mathrm{D2D}} = Y$.

In general, CGAN describes a minimum-maximum function (L_{CGAN}) between a generative model and a discriminative model as follows [49]:

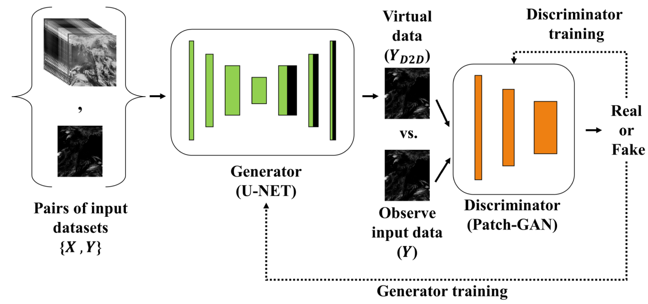

Fig. 3. CGAN structure of generator and discriminator in the D2D model.

$$L_{\mathrm{CGAN}} = E[\log(D(Y_{\mathrm{D2D}}, Y))] + E[\log(1 - D(Y, Y_{\mathrm{D2D}}))] \quad (3)$$

where X and Y are the pairs of true input data for CGAN. G attempts to minimize $\log(D(Y_{\mathrm{D2D}}, Y))$ in the first cross entropy, while D attempts to maximize the probability of discriminating real or virtual data in the second cross entropy. The log function was introduced in cross entropies to the efficient gradient at the initial step of model training [49].

The reconstruction loss (L_1) equation [50] is required to minimize the distance between the true output dataset (Y) and the generated dataset (Y_{D2D}). The (L_1) is obtained as follows:

$$L_1(G) = E(||Y - Y_{\mathrm{D2D}}||_1). \quad (4)$$

The loss function in D2D (L_{D2D}) consists of the adversarial and reconstruction loss as follows:

$$L_{\mathrm{D2D}} = \min_G \max_D \{L_{\mathrm{CGAN}}\} + \lambda \cdot L_1 \quad (5)$$

where λ is the parameter that demonstrates the tradeoff between the adversarial and reconstruction loss. This article set $\lambda = 1$.

Fig. 3 shows the CGAN structure in the D2D model. Green and orange boxes represent feature maps, while black boxes denote the copied feature maps and padding steps, respectively.

The GK-2A/AMI LWIR band TB and TB difference data were used as X, and GK-2A/AMI 1.37 μm band albedo as Y, for training and validation of the D2D model. For applying the D2D model, we used the Himawari/AHI LWIR band TB and TB difference data, as X. Finally, we obtained the virtual Himawari/AHI 1.37 μm band albedo (Y_{D2D}).

The proposed D2D model underwent approximately 41 h of training. The experiment was implemented on top of TensorFlow and optimized with the Adam optimizer [65] with Python 3.54 on CUDA 10.0 and cuDNN 7.5.17 systems running on one NVIDIA GeForce RTX 2080 Ti and an Intel Xeon CPU.

B. Multiband Selection for 1.37 μm D2D Model

The cirrus, located at the highest altitude compared to other clouds, predominantly contributes to cooling the upper troposphere through the radiative transfer, including emission and scattering of constituent ice particles [66]. The radiative effects of the cirrus in the far-IR bands are approximately double that in the LWIR bands [66].

TABLE II
CORRELATION COEFFICIENTS BETWEEN THE AMI 1.37 μM AND THE OTHER 6 AMI BANDS, 15 BRIGHTNESS TEMPERATURE DIFFERENCES

Band or Band difference (μm)	Jul. 2019	Aug. 2019	Sep. 2019	Oct. 2019	Nov. 2019	Dec. 2019	Jan. 2020	Feb. 2020	Mar. 2020	Apr. 2020	May 2020	Jun. 2020	Jul. 2020
IR9.6-IR10.5	0.8573	0.8456	0.7955	0.8177	0.7881	0.7036	0.7259	0.7429	0.7992	0.7773	0.8144	0.8413	0.8515
IR9.6-IR8.7	0.8590	0.8520	0.7960	0.8125	0.7791	0.6989	0.7203	0.7295	0.7897	0.7699	0.8165	0.8462	0.8590
IR9.6-IR11.2	0.8456	0.8327	0.7809	0.8097	0.7901	0.7127	0.7339	0.7432	0.7968	0.7753	0.8085	0.8312	0.8387
IR12.3	0.8493	0.8447	0.8417	0.8303	0.7220	0.6341	0.6321	0.6605	0.7807	0.7838	0.8372	0.8482	0.8635
IR9.6-IR12.3	0.8258	0.8123	0.7517	0.7869	0.7775	0.7136	0.7313	0.7202	0.7780	0.7655	0.8030	0.8214	0.8239
IR11.2	0.8440	0.8391	0.8359	0.8244	0.7110	0.6220	0.6201	0.6543	0.7757	0.7785	0.8316	0.8426	0.8597
IR10.5	0.8424	0.8375	0.8341	0.8206	0.7012	0.6123	0.6099	0.6508	0.7737	0.7751	0.8312	0.8420	0.8604
IR8.7	0.8406	0.8358	0.8317	0.8153	0.6915	0.6064	0.6038	0.6419	0.7679	0.7693	0.8305	0.8417	0.8621
IR13.3	0.8595	0.8532	0.8443	0.8200	0.6880	0.5901	0.5797	0.5907	0.7460	0.7801	0.8471	0.8607	0.8772
IR13.3-IR12.3	0.7847	0.7733	0.7497	0.7704	0.7277	0.6681	0.6796	0.7341	0.7717	0.7165	0.7350	0.7674	0.7812
WV7.3	0.8664	0.8646	0.8460	0.7965	0.6381	0.5446	0.5274	0.5087	0.6990	0.7473	0.8391	0.8739	0.8884
IR13.3-IR11.2	0.7602	0.7511	0.7406	0.7580	0.6878	0.6175	0.6258	0.7031	0.7578	0.7051	0.7133	0.7443	0.7603
WV7.3-IR12.3	0.7506	0.7449	0.7357	0.7436	0.6904	0.6299	0.6316	0.7016	0.7374	0.6860	0.7111	0.7418	0.7552
WV7.3-IR11.2	0.7412	0.7362	0.7269	0.7352	0.6685	0.6028	0.6035	0.6833	0.7282	0.6789	0.6988	0.7311	0.7461
IR13.3-IR10.5	0.7266	0.7214	0.7179	0.7321	0.6437	0.5754	0.5809	0.6822	0.7376	0.6791	0.6818	0.7160	0.7311
WV7.3-IR10.5	0.7288	0.7259	0.7149	0.7214	0.6443	0.5801	0.5798	0.6722	0.7169	0.6644	0.6838	0.7203	0.7355
WV7.3-IR8.7	0.7085	0.7084	0.6968	0.7019	0.6204	0.5661	0.5652	0.6570	0.6990	0.6435	0.6659	0.7036	0.7211
IR8.7-IR10.5	0.7196	0.6882	0.6859	0.7243	0.6620	0.5499	0.5391	0.5968	0.6771	0.6787	0.6501	0.6781	0.6812
IR13.3-IR8.7	0.6740	0.6720	0.6768	0.6905	0.5961	0.5489	0.5533	0.6545	0.7044	0.6378	0.6371	0.6702	0.6872
WV7.3-IR13.3	0.6834	0.6783	0.6419	0.6402	0.5735	0.5177	0.5199	0.5972	0.6153	0.5907	0.6197	0.6714	0.6866
IR8.7-IR11.2	0.5375	0.5253	0.5512	0.6354	0.6565	0.5841	0.5748	0.5785	0.6356	0.6388	0.5863	0.5495	0.5258

The radiative properties of cirrus clouds are primarily characterized using optical parameters such as the extinction optical thickness (τ), single-scattering albedo (ω), and asymmetry factor (g). These properties depend on microphysical factors such as particle size distribution and concentration profile in addition to the geometry and thickness of the cirrus cloud [66]. For example, the extinction optical thickness τ is described as follows [67], [68]:

$$\tau = \frac{3}{2}\overline{Q_e}\frac{\mathrm{IWP}}{D_e \rho_i} \tag{6}$$

where IWP is the ice water path (i.e., the column ice mass per unit area (g/m^2)), $\overline{Q_e}$ is the mean value of the extinction efficiency, D_e is the effective particle diameter, and ρ_i is the ice density. Note that $\overline{Q_e}$, and D_e are generally modeled [69], [70], [71], [72].

Thus, based on the different sensitivity of the cirrus clouds to different IR bands, this article tested the proper IR bands and the differences between the different bands for the proposed D2D model. Notably, this article only considered the LWIR bands because these bands observe the emission from the earth's clouds and surfaces, irrespective of day and night.

For the D2D model, to generate a D2D-based GK-2A/AMI and Himawari/AHI 1.37 μm band, we aim to find the best pair of GK-2A/AMI 1.37 μm and other VIS and IR bands by estimating the best correlation coefficient (CC) values >0.5 between these two bands or the differences in the IR band. Table II summarizes the monthly-averaged CCs (>0.5) found between the AMI 1.37 μm band and the other 6 AMI bands (7.3, 8.7, 10.5, 11.2, 12.3, and 13.3 μm) and the 15 difference between the TBs of 7.3–8.7 μm, 7.3–10.5 μm, 7.3–11.2 μm, 7.3–12.3 μm, 7.3–13.3 μm, 8.7–10.5 μm, 8.7–11.2 μm, 9.6–8.7 μm, 9.6–10.5 μm, 9.6–11.2 μm, 9.6–12.3 μm, 13.3–8.7 μm, 13.3–10.5 μm, 13.3–11.2 μm, and 13.3–12.3 μm. The monthly-averaged CC values were computed at 04:00 UTC from July 24, 2019 to July 31, 2020.

For example, 10.5 and 11.2 μm bands in the atmospheric window have sensitivities to clouds and aerosols in the atmosphere [73], [74]. The difference between 9.6 and 10.5 μm bands is used to indicate very high clouds and the influence of ozone absorption [75]. The difference between 8.7 and 10.5 μm bands is used to indicate thin, very high ice clouds [76], whereas that between 8.7 and 11.2 μm bands is used for differentiating between the cloud size particles [19], [77]. The 7.3 μm band is mainly sensitive to the distribution and amount of WV in the upper atmosphere. The difference between 12.3 and 13.3 μm effectively detects the rainfall region amidst thick cirrus [78]. Thus, the difference between 7.3 and 11.2 μm bands is used to differentiate the cumuliform clouds [79]. Notably, in this article, VIS, SWIR, and MWIR bands and a single 9.6 μm band were excluded because of their low CC (< 0.5) and dependence on sunlight. Additionally, VIS bands observe cirrus clouds and lower clouds. The red band is sensitive to the land surfaces. Thus, the CC values between VIS and 1.37 μm were lower than 0.5.

Fig. 4 shows the paired AMI 1.37 μm band with AMI 21 bands and BTDs datasets for training, validation, and application for our D2D model.

C. Pre- and Postprocesses for D2D

For preprocessing, all the original L1B datasets observed in the 21 bands, as well as band differences of AMI and AHI sensors, were resampled in 2 km $\times$ 2 km spatial resolution corresponding to 1024 $\times$ 1024 pixels. The resampled data were saved in the numerical array form, such as the npy format. The numerical and resampled datasets were converted to normalized numerical datasets in the range [−1, 1] owing to the use of hyperbolic tangent activation function ($tanh$) in the output layer in the U-Net encoder–decoder generator G model in the Pix2Pix as follows [80]:

$$X' = 2 \times \frac{X - X_{\min}}{X_{\max} - X_{\min}} - 1 \tag{7}$$

$$Y' = 2 \times \frac{Y - Y_{\min}}{Y_{\max} - Y_{\min}} - 1 \tag{8}$$

$$x_{\min} \leq x_i \leq x_{\max} \in X \ \rightarrow -1 \leq x'_i \leq 1 \in X' \tag{9}$$

$$y_{\min} \leq y_i \leq y_{\max} \in Y \ \rightarrow -1 \leq y'_i \leq 1 \in Y' \tag{10}$$

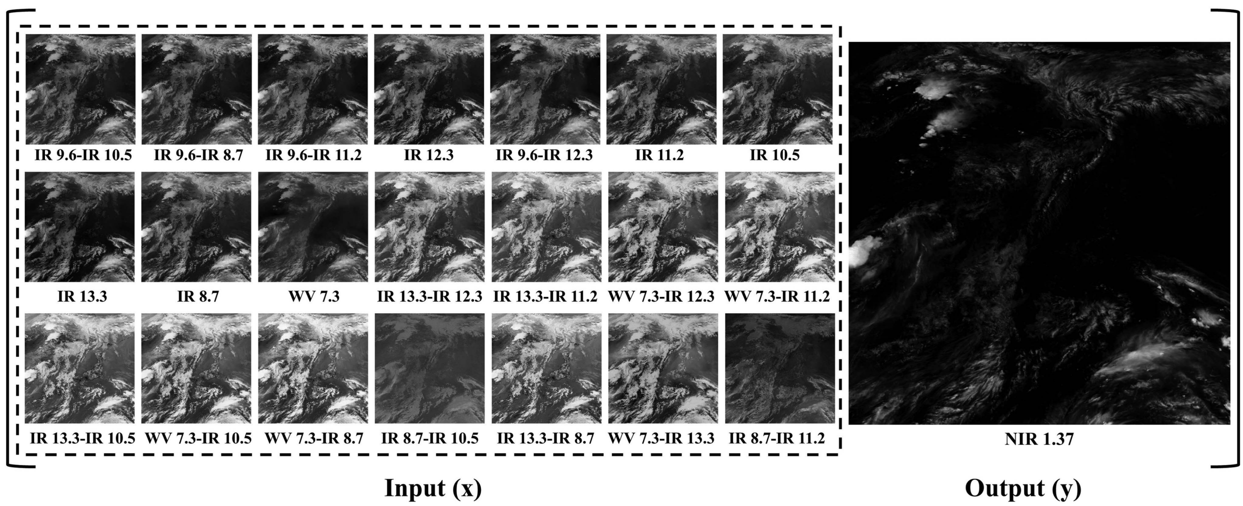

Fig. 4. Example of training pairs at 21 AMI IR bands and their differences and AMI 1.37 μm band on July 24, 2019, at 04:00 UTC.

where X' and Y' are the datasets of the normalized real-observed data x'_i and y'_i, respectively; and $x_{\min}$, $x_{\max}$, $y_{\min}$, and $y_{\max}$ are the minimum and maximum values of the real-observed data x_i and y_i, respectively.

Thus, the pairs of input datasets (X', Y') for training and validation for the D2D model were expressed as follows:

$$
\begin{aligned}
X' = x'_i \in \{ & R'_{7.3}, R'_{8.7}, R'_{10.5}, R'_{11.2}, R'_{12.3}, R'_{13.3} \\
& R'_{7.3} - R'_{8.7}, R'_{7.3} - R'_{10.5}, R'_{7.3} - R'_{11.2}, R'_{7.3} - R_{12.3} \\
& R'_{7.3} - R'_{13.3}, R'_{8.7} - R'_{10.5}, R'_{8.7} - R'_{11.2}, R'_{9.6} - R'_{8.7} \\
& R'_{9.6} - R'_{10.5}, R'_{9.6} - R'_{11.2}, R'_{9.6} - R'_{12.3}, R'_{13.3} - R'_{8.7} \\
& R'_{13.3} - R'_{10.5}, R'_{13.3} - R'_{11.2}, R'_{13.3} - R'_{12.3}, \}
\end{aligned}
\tag{11}
$$

$$
Y' = y'_i \in \{R'_{1.37}\} \tag{12}
$$

where R' is the normalized TB and albedo. The subscripts denote the central wavelength in the band.

After the D2D model development, output datasets (Y'_{D2D}) were obtained after applying the D2D model to other input datasets in the form of the normalized numerical array ranging from -1 to 1. Finally, the output datasets were denormalized into the range of original datasets in the 1.37 μm band for the postprocess as follows:

$$
Y_{\mathrm{D2D}} = Y_{\min} + \frac{Y'_{\mathrm{D2D}} + 1}{2} \times (Y_{\max} - Y_{\min}). \tag{13}
$$

Fig. 5 presents the procedure of D2D model processing and summarizes the preprocess, model training process, and postprocess for D2D. X_{TB} values are the TB or the differences between TB in the LWIR bands; and Y_{albedo} is the daytime albedo observed in the GK-2A/AMI 1.37 μm band. Table III summarizes $X_{\min}$, $X_{\max}$, $Y_{\min}$, and $Y_{\max}$.

In preprocessing, training datasets were normalized between -1 and 1. In the model training process, the generator and discriminator were trained by their weights. In the postprocess, the simulation results of the D2D-generated AMI 1.37 μm band were denormalized to the range of original AMI observations.

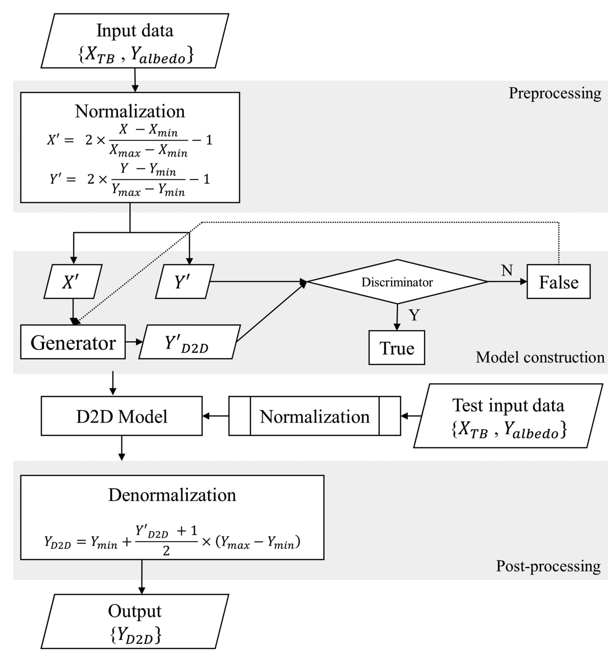

Fig. 5. Schematic of D2D model processing to generate AHI 1.37 μm band albedo from training to application.

Finally, the denormalized D2D-AHI 1.37 μm band was compared with the observed AMI 1.37 μm band in the same target areas.

D. Training, Validation, and Application of the D2D Model

For training our D2D model, the input patches of GK-2A/AMI from July 24, 2019 to July 31, 2020, at 04:00 UTC were trimmed to a size of 1024 $\times$ 1024 pixels in a batch size of 334. The AMI data are available from July 24, 2019. Thus, this article used the AMI data for one year from that date as a training dataset. This article selected a time of 04:00 UTC (13:00 Korean Standard Time) for obtaining the data to maximize the sunlight effect. Thus, for model training, D used a batch of 334 AMI

TABLE III
MIN AND MAX PARAMETERS FOR DATASET NORMALIZATION

X Datasets Ranges		
Band or Band difference (μm)	Min (K)	Max (K)
7.3μm	185.3228	290.4313
8.7μm	188.1435	312.5371
10.5μm	186.5613	316.3202
11.2μm	186.0126	315.7710
12.3μm	186.3793	311.4091
13.3μm	188.8179	283.5692
7.3μm–8.7μm	–55.3465	58.4013
7.3μm–10.5μm	–60.9633	58.2909
7.3μm–11.2μm	–61.2838	59.0455
7.3μm–12.3μm	–55.4100	59.5477
7.3μm–13.3μm	–34.6448	59.8061
8.7μm–10.5μm	–16.4445	15.9948
8.7μm–11.2μm	–14.4084	20.4729
9.6μm–8.7μm	–48.6420	21.2197
9.6μm–10.5μm	–53.6286	22.8018
9.6μm–11.2μm	–54.2952	23.3505
9.6μm–12.3μm	–49.6541	23.2320
13.3μm–8.7μm	–36.3194	7.8588
13.3μm–10.5μm	–37.6221	6.5632
13.3μm–11.2μm	–36.9007	7.2042
13.3μm–12.3μm	–31.9083	6.4847
Y Datasets Ranges		
Band or Band difference (μm)	Min (%)	Max (%)
1.37μm	–0.0033	0.6917

1.37 μm band albedo datasets of 1024 $\times$ 1024 pixels. G used a batch of 334 bright temperatures of the same size in 6 AMI bands (7.3, 8.7, 10.5, 11.2, 12.3, and 13.3 μm) and 15 AMI bands difference between the bright temperatures (7.3–8.7 μm, 7.3–10.5 μm, 7.3–11.2 μm, 7.3–12.3 μm, 7.3–13.3 μm, 8.7–10.5 μm, 8.7–11.2 μm, 9.6–8.7 μm, 9.6–10.5 μm, 9.6–11.2 μm, 9.6–12.3 μm, 13.3–8.7 μm, 13.3–10.5 μm, 13.3–11.2 μm, and 13.3–12.3 μm). During this process, our D2D model was trained to resemble the D2D-generated virtual albedo at AMI 1.37 μm band to the observed albedo at AMI 1.37 μm band, and for the discriminator D to distinguish the observed albedo from the D2D-generated albedo at AMI 1.37 μm band.

Thirty-seven pairs of the AMI 1.37 μm band and the superposition with 21 TBs and BTD data were used to validate the optimal iteration number for D2D model construction. The validation data periods were from the 1st, 15th, and 28th of each month (July 28, 2019 to October 1, 2020), which were not included in the training datasets. The D2D model was applied to the Himawari-8/AHI sensor with 36 datasets, the superposition of 21 combinations of AHI TBs and BTDs. The AHI data periods were each month's 1st, 15th, and 28th from January 2020 to December 2020. Finally, D2D-generated Himawari-8/AHI 1.37 μm data were compared with the observed GK-2A/AMI 1.37 μm data for the same dates as the AHI simulations.

E. Statistical Comparison

The D2D-generated AMI and AHI 1.37 μm bands were compared with the observed AMI 1.37 μm band using CC, bias, root-mean-square-error (RMSE), index of agreement (IA), mean absolute error (MAE), relative mean bias error (rMBE), and relative RMSE (rRMSE) as follows [81], [82]:

$$\mathrm{CC} = \frac{\sum_{i=1}^{N}\left(R_{\mathrm{AI},i}-\overline{R_{\mathrm{AI}}}\right)\left(R_{\mathrm{Real},i}-\overline{R_{\mathrm{Real}}}\right)}{\sqrt{\sum_{i=1}^{N}\left(R_{\mathrm{AI},i}-\overline{R_{\mathrm{AI}}}\right)^2}\sqrt{\sum_{i=1}^{N}\left(R_{\mathrm{Real},i}-\overline{R_{\mathrm{Real}}}\right)^2}} \tag{14}$$

$$\mathrm{Bias} = \frac{1}{N}\sum_{i=1}^{N}\left(R_{\mathrm{AI},i}-R_{\mathrm{Real},i}\right) \tag{15}$$

$$\mathrm{RMSE} = \sqrt{\frac{1}{N}\sum_{i=1}^{N}\left(R_{\mathrm{AI},i}-R_{\mathrm{Real},i}\right)^2} \tag{16}$$

$$\mathrm{IA} = 1-\frac{\sum_{i=1}^{N}\left(R_{\mathrm{AI},i}-\overline{R_{\mathrm{Real}}}\right)^2}{\sum_{i=1}^{N}\left(\left|R_{\mathrm{Real},i}-\overline{R_{\mathrm{AI}}}\right|+\left|R_{\mathrm{AI},i}-\overline{R_{\mathrm{AI}}}\right|\right)^2} \tag{17}$$

$$\mathrm{MAE} = \frac{1}{N}\sum_{i=1}^{N}\left(\left|R_{\mathrm{AI},i}-R_{\mathrm{Real},i}\right|\right) \tag{18}$$

$$\mathrm{rMBE} = \frac{\frac{1}{N}\sum_{i=1}^{N}\left(R_{\mathrm{AI},i}-R_{\mathrm{Real},i}\right)}{\overline{R_{\mathrm{Real}}}} \tag{19}$$

$$\mathrm{rRMSE} = \frac{\sqrt{\frac{1}{N}\sum_{i=1}^{N}\left(R_{\mathrm{AI},i}-R_{\mathrm{Real},i}\right)^2}}{\overline{R_{\mathrm{Real}}}} \tag{20}$$

where i is the index from 1 to N, N is the total number of pixels in the AMI data, $R_{\mathrm{Real},i}$ denotes the albedo of an ith pixel in the observed AMI, and $R_{\mathrm{AI},i}$ denotes the albedo of ith pixel in the D2D-generated AMI. $\overline{R_{\mathrm{Real}}}$ and $\overline{R_{\mathrm{AI}}}$ are the mean albedo values of observed AMI and D2D-generated AMI (or AHI) data, respectively.

In addition, the D2D model was validated using traditional stochastic skill scores, including the probability of detection (POD) for a correct prediction, false alarm ratio (FAR) for false prediction, proportion correct (PC), critical success index (CSI), and Heidke skill score (HSS) [81]. The POD, FAR, CSI, and HSS were calculated as follows:

$$\mathrm{POD} = \frac{A}{A+C} \tag{21}$$

$$\mathrm{FAR} = \frac{B}{A+B} \tag{22}$$

$$\mathrm{PC} = \frac{(A+D)}{\mathrm{A+B+C+D}} \tag{23}$$

$$\mathrm{CSI} = \frac{A}{A+B+C} \tag{24}$$

$$\mathrm{HSS} = 2\frac{(AD-BC)}{\left[(A+C)(C+D)+(A+B)(B+D)\right]} \tag{25}$$

where A is the hit (the number of D2D-generated AHI cirrus pixels corresponding to observed AMI cirrus pixels), B is the miss (the number of D2D-generated AHI cirrus pixels that do not correspond to observed AMI cirrus pixels, or the number of false alarms), C is the number of false alarms (the number of no D2D-generated AHI cirrus pixels corresponding to observed AMI cirrus pixels, or the number of misses), and D is the correct

TABLE IV
2 × 2 CONTINGENCY TABLE

2×2 Contingency Table	AMI cirrus pixel (Yes)	AMI cirrus pixel (No)
D2D-AHI cirrus pixel (Yes)	*A*	*B*
D2D-AHI cirrus pixel (No)	*C*	*D*

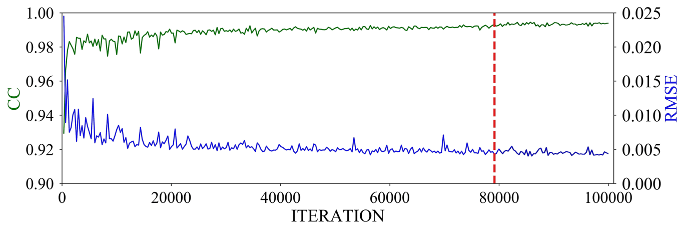

Fig. 6. CC and RMSE between the observed AMI 1.37 μm band albedo and the D2D-generated band on December 1, 2019.

nonevent (the number of no D2D-generated AHI cirrus pixels corresponding to no real AMI cirrus pixels, or the number of correct rejections). Table IV summarizes the contingency tables.

IV. RESULTS

A. Hypothetical AMI 1.37 μm Band

Fig. 6 shows the variations in the CC and RMSE values during the iterative model training between the observed and D2D-generated AMI 1.37 μm band albedo and the D2D model in the validation datasets. The D2D model showed a maximum CC value of 0.9931 and a minimum RMSE value of 0.0043 around December 1, 2019. The most common number of iterations in the validation datasets is 79158. Thus, this iteration trained model was adopted as the constructed D2D model to simulate the albedo in the 1.37 μm GK-2A/AMI and Himawari-8/AHI sensors.

Fig. 7 shows the results of one of the validation datasets to our model for AMI. Fig. 7(a) and (b) shows the observed GK-2A/AMI and D2D-generated GK-2A/AMI 1.37 μm band albedo, respectively, from September 28, 2019, 04:00 UTC. Fig. 7(c) shows the differences between the observed and D2D-generated AMI 1.37 μm band, from −0.15 to 0.15 (albedo). The D2D-generated model produced an excellent spatial distribution of the observed AMI 1.37 μm band. Fig. 7(d) shows the AMI true-color RGB image obtained using the AMI red, green, and blue bands simultaneously. As can be seen, our model-generated AMI 1.37 μm band albedo is qualitatively accurate.

Fig. 8 shows the scatterplot between the observed AMI and D2D-generated AMI 1.37 μm band albedo with CC = 0.9948, bias = 0.0007, RMSE = 0.0079, rMBE = 0.0211%, and rRMSE = 0.235%. This comparison demonstrates the excellent accuracy of the proposed D2D model.

B. Hypothetical AHI 1.37 μm Band

Fig. 9 shows the results when one of the datasets was applied to our D2D model for AHI observations. Fig. 9(a) and (b) shows the observed GK-2A/AMI and D2D-generated Himawari/AHI 1.37 μm band albedo, respectively, on February 28, 2020, 04:00 UTC. As mentioned, no real Himawari/AHI 1.37 μm band

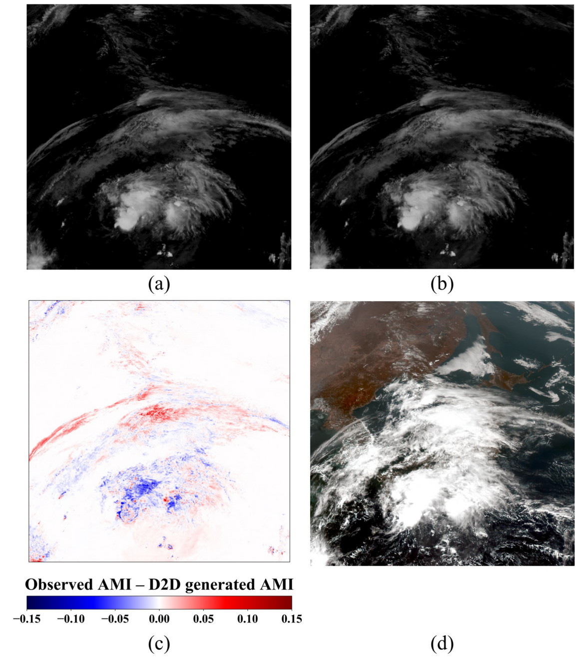

Fig. 7. (a) Observed AMI 1.37 μm band. (b) D2D-generated AMI 1.37 μm band. (c) Difference between (a) and (b) from −0.15 to 0.15 (albedo). (d) AMI true color RGB image using 0.47, 0.51, and 0.64 μm bands. The time is September 28, 2019, at 04:00 UTC.

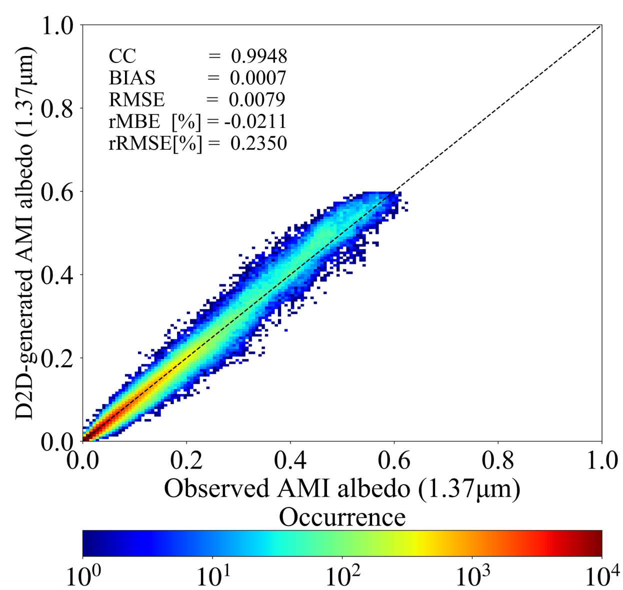

Fig. 8. Scatterplots between the observed AMI and the D2D-generated AMI 1.37 μm band albedo on September 28, 2019, at 04:00 UTC.

albedo is available; therefore, this article used AMI 1.37 μm band albedo in the common study area to compare. Fig. 9(a) and (b) shows the general features of cirrus clouds in this article area and the qualitative accuracy of the proposed D2D-generated AHI 1.37 μm band albedo. Fig. 9(c) shows the difference between observed AMI and D2D-generated AHI 1.37 μm band, from −0.15 to 0.15 (albedo). Fig. 9(d) shows the AMI true-color RGB image. Compared with the D2D-generated AMI albedo in Fig. 7, the D2D-generated AHI albedo intensity appears to be

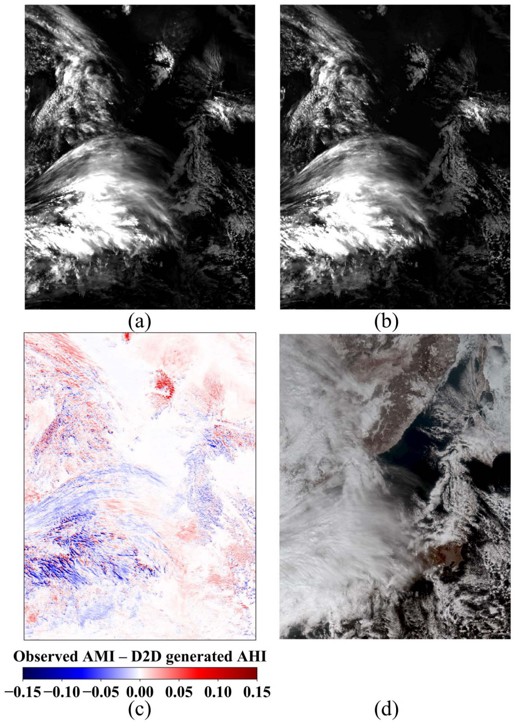

Fig. 9. (a) Observed AMI. (b) D2D-generated AHI. (c) Difference between (a) and (b) from −0.15 to 0.15 (albedo). (d) AMI true color RGB image using 0.47, 0.51, and 0.64 μm bands. The time is February 28, 2020, at 04:00 UTC.

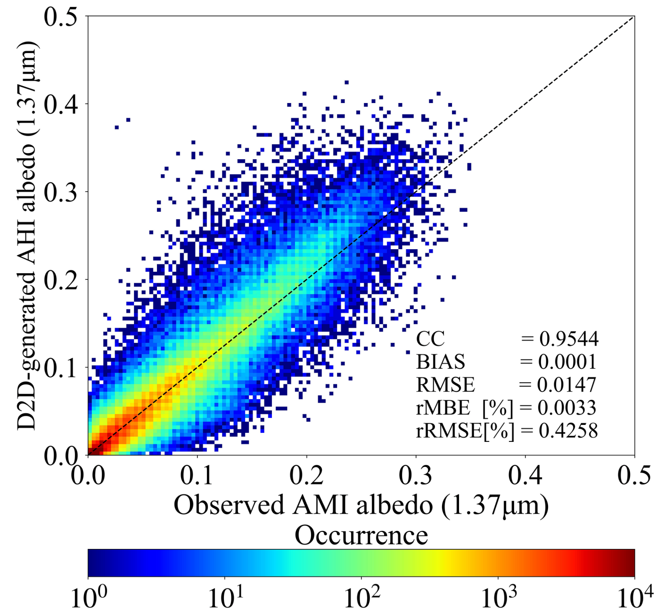

Fig. 10. Scatterplots between the observed AMI and the D2D-generated AHI 1.37 μm band albedo on February 28, 2020, at 04:00 UTC.

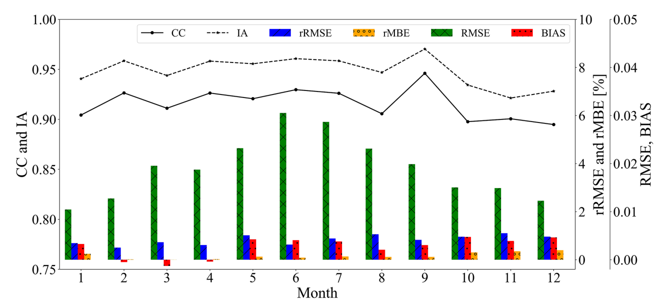

Fig. 11. Time-series results of the average values of CC, IA, bias, RMSE, rMBE, and rRMSE between the observed AMI 1.37 μm band and the D2D-generated AHI 1.37 μm band albedo on the 1st, 15th, and 28th of each month of 2020.

higher than the observed AMI albedo. These differences may be related to AMI and AHI sensors' different geometrical locations and SRFs in IR bands. The virtual AHI albedo was created by applying the AHI data to the pretrained D2D model constructed using AMI data. The transfer learning from AMI to AHI sensors may lead to relatively lower accuracy in the D2D-generated AMI albedo shown in Fig. 7 than in D2D-generated AHI albedo shown in Fig. 9.

Fig. 10 shows the scatterplots between the observed AMI and D2D-generated AHI 1.37 μm band albedo in Fig. 9. The bias, RMSE, and CC between the two data are −0.0001, 0.0147, and 0.9544, respectively, in albedo. The rMBE and rRMSE show 0.0046%, and 0.42%, respectively. Thus, a good agreement between them can be identified. Notably, the D2D-generated AHI 1.37 μm band shows a little overestimation as the albedo increases. This result was due to missing input datasets such as solar and satellite zenith angles and relative azimuth angles of AMI and AHI sensors. Additionally, the effect of the transfer learning (from AMI to AHI sensors) on the AHI sensor using the pretrained D2D model with AMI data affected the result.

Fig. 11 shows the statistical results of comparison between the observed AMI 1.37 μm band albedo and the D2D-generated AHI 1.37 μm band albedo with the average values from the January 1st, 15th, and 28th, 2020, 04:00 UTC, to December 2020, 04:00 UTC. The CC values ranging from 0.8948 to 0.9461 were relatively stable during the year. The bias and RMSE ranged from −0.0013 to 0.0047, and from 0.0104 to 0.0305, respectively. The bias and RMSE increased from January to June but decreased from June to December. The RMSE shows the highest relative value in June because of a relatively larger area of cirrus compared with other months. This result is related to the presence of more cirrus clouds in this region owing to high pressures from the continental air mass over the Yangtze River in spring, and typhoons in summer. Referring to [82], models based on rMBE and rRMSE values can be classified as excellent ($|\text{rMBE}| < 2\%$ and $|\text{rRMSE}| < 5\%$), good ($2\% < |\text{rMBE}| < 5\%$ and $5\% < |\text{rRMSE}| < 10\%$), average ($5\% < |\text{rMBE}| < 10\%$ and $10\% < |\text{rRMSE}| < 15\%$), and poor ($10\% < |\text{rMBE}|$ and $15\% < |\text{rRMSE}|$) models. The D2D model showed that rMBE and rRMSE ranged less than 2%. The IA shows a similar pattern to CC values. These results demonstrate very high accuracy and low error on the D2D-generated AH+.1.37 μm band albedo compared with the observed AMI 1.37 μm band albedo.

Fig. 12 shows the statistical comparison results between the observed AMI and the D2D-generated AHI 1.37 μm band albedos with the average values on every 1st, 15th, and 28th day of the month from January 2020, 04:00 UTC, to December 2020, 04:00 UTC. The D2D-generated AHI 1.37 μm band showed consistent results for POD (0.8990 to 0.9650), FAR (0.0627 to

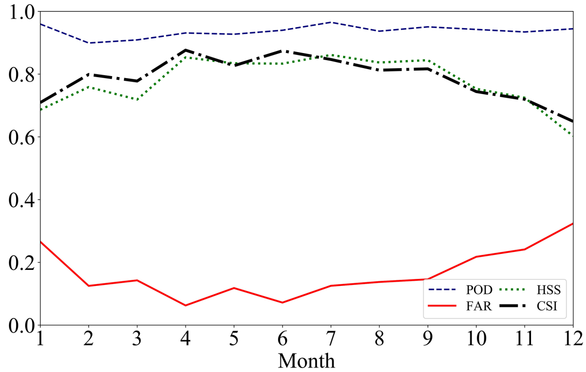

Fig. 12. Time-series results of the POD, FAR, HSS, and CSI values between the observed AMI 1.37 μm band and the D2D-generated AHI 1.37 μm band albedo with the average values on every 1st, 15th, and 28th of each month in 2020.

0.3238), HSS (0.6027 to 0.8609), and CSI (0.6493 to 0.8761). The CSI and HSS value had a similar pattern to CC and IA. CSI and HSS decreased from October to December, and POD and FAR increased. The FAR values showed the opposite tendency to the CSI and HSS values. The POD values were relatively over 0.89. During winter, the 1.37 μm band detected lower clouds in a dry atmosphere [83], which may be responsible for a higher FAR value from November to January.

C. Validation With CALIPSO Data

Fig. 13 shows the comparison results for cirrus detection between CALIPSO and AMI or AHI 1.37 μm bands. Fig. 13(a) shows the comparison (lines) between CALIPSO and AMI cirrus detection with the TBs at the AMI 1.37 μm band (background image). Fig. 13(b) shows the comparison result between CALIPSO and D2D-generated AHI cirrus detection. The blue color denotes that both CALIPSO and the 1.37 μm bands detected cirrus cloud. The orange color indicates no cirrus in both CALIPSO and 1.37 μm bands. The green pixels indicate that only CALIPSO detected cirrus clouds. The yellow pixels indicate that only the AHI or AMI 1.37 μm bands detected cirrus cloud. In this comparison, a threshold value of 0.007 was applied to the AHI and AMI 1.37 μm bands, which was the MODIS-derived threshold for the 1.37 μm band for cirrus detection [59].

Fig. 14 shows the CALIPSO VFM data for the case shown in Fig. 13. Nine different flags are shown in the legend. We chose the cirrus flag for the comparison. Additionally, we compared the D2D-generated AHI cirrus data with the CALIPSO VFM cirrus data during 2020 when CALIPSO passed between Korea and Japan. We obtained 16 cases of spatiotemporal collocation between the two datasets within the study area. The average statistical results between CALIPSO and D2D-generated AHI data gave a POD = 0.8250, FAR = 0.4265, HSS = 0.3903, CSI = 0.5020, and PC = 0.7070. However, the average statistical results between CALIPSO and observed AMI data gave a POD = 0.7181, FAR = 0.3963, HSS = 0.3847, CSI = 0.4774, and PC = 0.7198. These results demonstrate that the D2D-generated AHI 1.37 μm band performed similarly to the observed AMI 1.37 μm. Notably, previous studies showed that the MODIS cloud algorithm for thin clouds gave a POD = 0.849, FAR = 0.091 [84], and PC = 0.881 [85]. The AMI cloud algorithm gave a POD = 0.652 and FAR = 0.289 [86]. Notably, the accuracy of the observed AMI and D2D-generated AHI cirrus bands depended on the threshold value of the MODSI cloud algorithm. This result could be improved by further study.

V. Discussion

This article proposes a D2D method to simulate a virtual AHI 1.37 μm band albedo using GK-2A/AMI 1.37 μm band and superposition of 21 AMI LWIR bands and band differences. Because of the capability to present a physically nonexistent observation by a real satellite but physically reasonable information using deep-learning techniques, this article significantly contributes to the satellite remote sensing community. Thus, the D2D method used in this article can complement the band information required for a variety of satellite application products and algorithms based on a multiband combination. This article demonstrated this advantage from a low difference between the observed AMI 1.37 μm and D2D-generated AHI 1.37 μm. Our results showed that the deep-learning technique could simulate the AHI 1.37 μm band, which can be helpful to identify meteorological features from stationary land features [83] and detect cirrus clouds for the Himawari-8/AHI.

This article appears to be similar to a previous study [54] for virtual green band generation of ABI sensor in the GOES-R satellite, as both studies generated nonexistent bands of weather satellites. However, this article used a quantitative data translation method from IR bands to a NIR band, whereas the previous study [54] used a qualitative image-to-image translation between VIS and other VIS bands.

One limitation of this article was the dependence on highly correlated bands of the own satellite and the neighboring satellites with similar bands. This article used 21 combinations of IR bands and their difference from the original 16 bands. This article could provide more accurate results if the AMI and AHI sensors have other bands sensitive to cirrus. However, other bands are not available.

Furthermore, the proposed D2D method tends to overestimate the virtual AHI 1.37 μm band compared to the observed AMI 1.37 μm band. This feature could result from the transfer learning of the D2D model using the AMI data, different SRFs between the two sensors, and different solar effects due to the separated longitudinal locations between AMI and AHI sensors. Thus, the D2D-generated AHI 1.37 μm band derived the overestimation of cirrus pixels, in particular, at the edges of cirrus clouds.

Another limitation encountered in this article was in producing the time-varying virtual AHI 1.37 μm band because the D2D model was constructed using the AMI datasets at a fixed time (04:00 UTC). However, the time-fixed D2D model has the advantage of generating the virtual AHI 1.37 μm band over a wide region, including the area with no solar reflection from sunrise to sunset, as if the solar angle is permanently fixed at

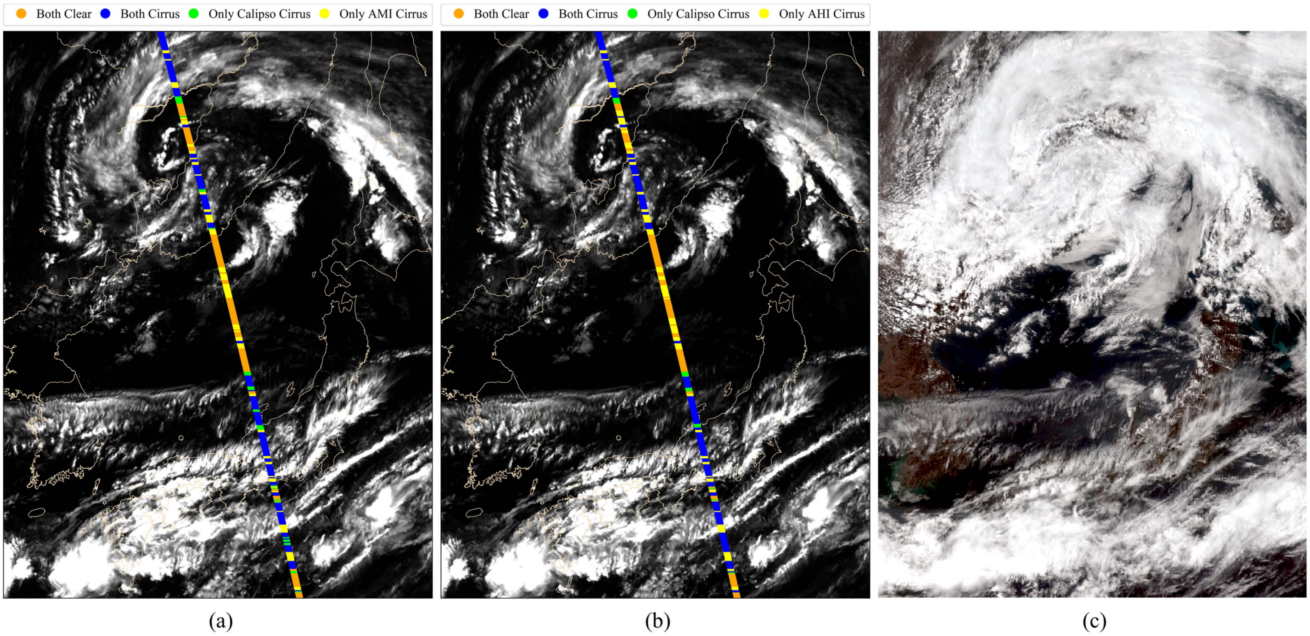

Fig. 13. Comparison between CALIPSO VFM data. (a) AMI 1.37 μm band. (b) D2-generated AHI 1.37 μm band. (c) Himawari RGB image on June 15, 2020, at 04:30 UTC.

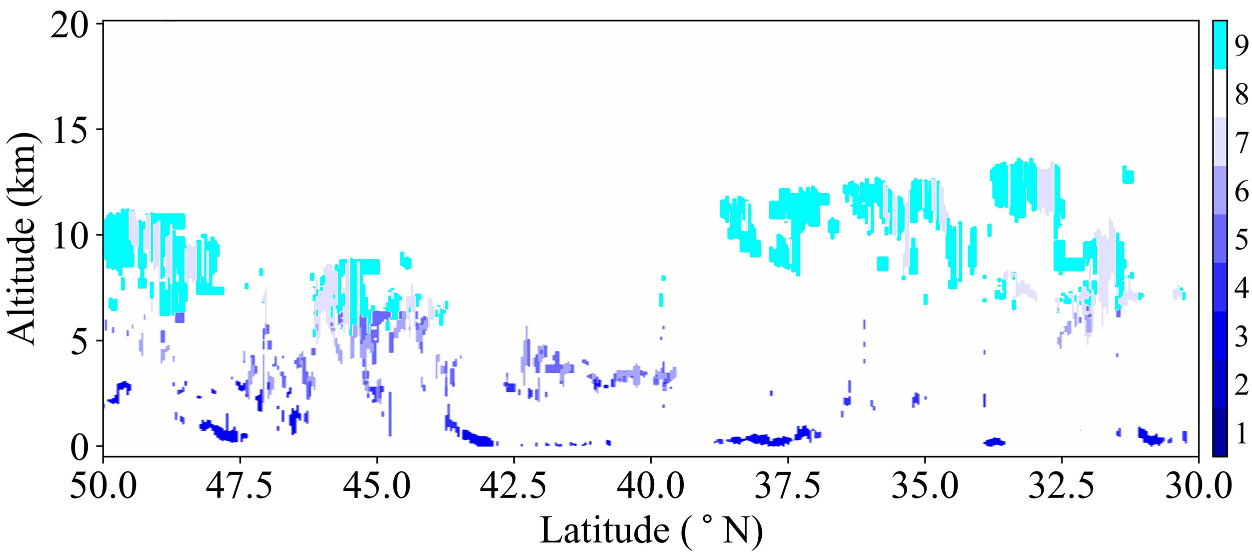

Fig. 14. CALIPSO VFM at altitudes from 0 to 20 km in the article area on June 15, 2020, at 04:30 UTC. The legend represents cloud types as nine flags. The cyan color indicates cirrus clouds, while white and blue colors indicate other types of cloud.

04:00 UTC. The construction of the time-varying D2D model is possible and will be the focus of future work. The preference for the temporal variation or wide-area observation will depend on the user's interests.

Additionally, this article did not include viewing conditions between AMI and AHI sensors, i.e., the relative location between the satellite and the cloud [87], affecting the albedo in VIS bands. Thus, further study using the solar and satellite zenith angles and relative azimuth angles as additional input datasets for the D2D model could improve the performance of the proposed D2D model.

Finally, this article has a deep-learning computational limitation in generating the full disk data with a high spatial resolution due to GPU memory intensiveness, despite rapid advances in hardware performance.

Despite a few limitations, this article proposed a beneficial capability for generating a nonexistent band of an existent satellite and producing virtual observation data in a region with no solar reflection, which was impossible in the traditional approaches. The presented D2D method could be applied to global cirrus monitoring, estimating the cloud effects on solar radiation and the energy balance of the earth, and long-term climate change studies using a combination of numerous real 1.37 μm bands onboard other geostationary weather satellites located at different longitudes, such as GOES-16/-17 and Meteosat Third Generation satellites.

Furthermore, the nonexistent AMI 2.2 μm band, like the nonexistent AHI 1.37 μm band, can be generated by a D2D method presented in this article. However, the virtual generation of missing bands such as the green band, 6.9 and 9.6 μm bands in the Fengyun-4 with 14 bands ranging from 0.45 to 13.8 μm band will be challenging for the proposed D2D method application using the neighboring GK-2A or Himawari-8 satellites.

VI. Summary and Conclusion

Geostationary satellites with VIS and IR bands have been crucial in monitoring weather, particularly in nowcasting and forecasting. Recently, geostationary weather satellites equipped with advanced meteorological imagers have been launched and put into operation. However, the AHI sensor onboard Himawari-8 does not have the 1.37 μm band, which is important for detecting thin cirrus clouds. Many previous studies have aimed to detect thin cirrus using the 1.37 μm band, such as the MODIS, VIIRS, OLI, and MSI sensors onboard polar orbit satellites, and cirrus has played a crucial role in the earth's radiation budget and the greenhouse effect

This article presents a D2D method to simulate a virtual AHI 1.37 μm band albedo using GK-2A/AMI 1.37 μm band and superposition of 21 AMI LWIR bands and band differences. The D2D model was trained to simulate an AMI 1.37 μm band via superposition of 21 AMI LWIR bands and band differences using Pix2Pix, to implement CGAN. The D2D-generated AMI 1.37 μm band albedo showed excellent statistical agreement with the observed AMI 1.37 μm band albedo. On the basis of excellent results in the hypothetical AMI sensor, the D2D model was applied to generate hypothetical AHI 1.37 μm band albedo translating the superposition of 21 AHI LWIR bands and band differences to the nonexistent AHI 1.37 μm band albedo. The observed AMI 1.37 μm band albedo and D2D-generated AHI 1.37 μm band albedo were compared, and the results showed good agreement, i.e., high CC and low RMSE between the two datasets. Additionally, the D2D-generated AHI 1.37 μm band showed similar accuracies to the observed AMI 1.37 μm band from the validation with the CALIPSO VFM data. Thus, the proposed D2D model could be extended to simulate missing bands in sensors onboard satellites and other optical satellite applications. Future work will address the nonexistent AMI 2.26 μm band simulation similar to the virtual AHI 1.37 μm band simulation.

Acknowledgment

The authors would like to thank anonymous reviewers' helpful and constructive comments on the manuscript. The GK-2A/AMI and Himawari-8 data used in this article were supplied by the NMSC of the KMA and JAXA, respectively.

References

[1] D. K. Lynch, "Cirrus: History and definition," in *Cirrus*, D. K. Lynch, K. Sassen, D. O'C. Starr, and G. Stephens, Eds. New York, NY, USA: Oxford Univ. Press, 2002.

[2] I. Schlimme, A. Macke, and J. Reichardt, "The impact of ice crystal shapes, size distributions, and spatial structures of cirrus clouds on solar radiative fluxes," *J. Atmos. Sci.*, vol. 62, no. 7, pp. 2274–2283, 2005, doi: 10.1175/JAS3459.1.

[3] D. L. Mitchell and W. Finnegan, "Modification of cirrus clouds to reduce global warming," *Environ. Res. Lett.*, vol. 4, no. 4, 2009, Art. no. 045102.

[4] C. J. Stubenrauch, A. Chédin, G. Rädel, N. A. Scott, and S. Serrar, "Cloud properties and their seasonal and diurnal variability from TOVS path-B," *J. Climate*, vol. 19, no. 21, pp. 5531–5553, 2006, doi: 10.1175/JCLI3929.1.

[5] K. Sassen, Z. Wang, and D. Liu, "Global distribution of cirrus clouds from CloudSat/Cloud-Aerosol lidar and infrared pathfinder satellite observations (CALIPSO) measurements," *J. Geophys. Res. Atmos.*, vol. 113, no. D8, 2008, Art. no. D00A12, doi: 10.1029/2008JD009972.

[6] H. Nazaryan, M. P. McCormick, and W. P. Menzel, "Global characterization of cirrus clouds using CALIPSO data," *J. Geophys. Res. Atmos.*, vol. 113, no. D16, 2008, Art. no. D16211, doi: 10.1029/2007JD009481.

[7] V. Ramaswamy and V. Ramanathan, "Solar absorption by cirrus clouds and the maintenance of the tropical upper troposphere thermal structure," *J. Atmos. Sci.*, vol. 46, no. 14, pp. 2293–2310, 1989.

[8] C. Poetzsch-Heffter, Q. Liu, E. Ruperecht, and C. Simmer, "Effect of cloud types on the earth radiation budget calculated with the ISCCP Cl dataset: Methodology and initial results," *J. Climate*, vol. 8, no. 4, pp. 829–843, 1995.

[9] T. Chen, W. B. Rossow, and Y. Zhang, "Radiative effects of cloud-type variations," *J. Climate*, vol. 13, no. 1, pp. 264–286, 2000.

[10] J. C. Dupont and M. Haeffelin, "Observed instantaneous cirrus radiative effect on surface-level shortwave and longwave irradiances," *J. Geophys. Res. Atmos.*, vol. 113, no. D21, 2008, Art. no. D21202, doi: 10.1029/2008JD009838.

[11] K.-N. Liou, "Influence of cirrus clouds on weather and climate processes: A global perspective," *Monthly Weather Rev.*, vol. 114, no. 6, pp. 1167–1199, 1986.

[12] B. C. Gao, A. F. Goetz, and W. J. Wiscombe, "Cirrus cloud detection from airborne imaging spectrometer data using the 1.38 μm water vapor band," *Geophys. Res. Lett.*, vol. 20, no. 4, pp. 301–304, 1993, doi: 10.1029/93GL00106.

[13] D. P. Wylie, W. P. Menzel, H. M. Woolf, and K. I. Strabala, "Four years of global cirrus cloud statistics using HIRS," *J. Climate*, vol. 7, no. 12, pp. 1972–1986, 1994.

[14] K. Hutchison and N. Choe, "Application of 1-38 μm imagery for thin cirrus detection in daytime imagery collected over land surfaces," *Int. J. Remote Sens.*, vol. 17, no. 17, pp. 3325–3342, 1996, doi: 10.1080/01431169608949154.

[15] S. Ou, K. Liou, M. King, and S. Tsay, "Remote sensing of cirrus cloud parameters based on a 0.63-3.7 μm radiance correlation technique applied to AVHRR data," *Geophys. Res. Lett.*, vol. 26, no. 16, pp. 2437–2440, 1999, doi: 10.1029/1999GL900554.

[16] P. Rolland, K. Liou, M. King, S. Tsay, and G. McFarquhar, "Remote sensing of optical and microphysical properties of cirrus clouds using moderate-resolution imaging spectroradiometer channels: Methodology and sensitivity to physical assumptions," *J. Geophys. Res. Atmos.*, vol. 105, no. D9, pp. 11721–11738, 2000, doi: 10.1029/2000JD900028.

[17] P. Rolland and K. Liou, "Surface variability effects on the remote sensing of thin cirrus optical and microphysical properties," *J. Geophys. Res. Atmos.*, vol. 106, no. D19, pp. 22965–22977, 2001, doi: 10.1029/2001JD900160.

[18] B.-C. Gao, P. Yang, W. Han, R.-R. Li, and W. J. Wiscombe, "An algorithm using visible and 1.38-/spl mu/m channels to retrieve cirrus cloud reflectances from aircraft and satellite data," *IEEE Trans. Geosci. Remote Sens.*, vol. 40, no. 8, pp. 1659–1668, Aug. 2002, doi: 10.1109/TGRS.2002.802454.

[19] J. Roskovensky and K. Liou, "Detection of thin cirrus from 1.38 μm/0.65 μm reflectance ratio combined with 8.6–11 μm brightness temperature difference," *Geophys. Res. Lett.*, vol. 30, no. 19, 2003, Art. no. 1985, doi: 10.1029/2003GL018135.

[20] B.-C. Gao and R.-R. Li, "Removal of thin cirrus scattering effects in Landsat 8 OLI images using the cirrus detecting channel," *Remote Sens.*, vol. 9, no. 8, p. 834, 2017, doi: 10.3390/rs9080834.

[21] J. Wei et al., "Cloud detection for Landsat imagery by combining the random forest and superpixels extracted via energy-driven sampling segmentation approaches," *Remote Sens. Environ.*, vol. 248, 2020, Art. no. 112005, doi: 10.1016/j.rse.2020.112005.

[22] E. Ben-Dor, "A precaution regarding cirrus cloud detection from airborne imaging spectrometer data using the 1.38 μm water vapor band," *Remote Sens. Environ.*, vol. 50, no. 3, pp. 346–350, 1994, doi: 10.1016/0034-4257(94)90084-1.

[23] J. M. Sieglaff and T. J. Schmit, "Vegetation monitoring and thin cirrus detection on the next generation GOES imager," in *Proc. 12th Conf. Satell. Meteorol. Oceanogr.*, Long Beach, CA, USA, 2003, p. 5.4.

[24] C. O. Justice et al., "The moderate resolution imaging spectroradiometer (MODIS): Land remote sensing for global change research," *IEEE Trans. Geosci. Remote Sens.*, vol. 36, no. 4, pp. 1228–1249, Jul. 1998, doi: 10.1109/36.701075.

[25] S. A. Ackerman, K. I. Strabala, W. P. Menzel, R. A. Frey, C. C. Moeller, and L. E. Gumley, "Discriminating clear sky from clouds with MODIS," *J. Geophys. Res. Atmos.*, vol. 103, no. D24, pp. 32141–32157, 1998, doi: 10.1029/1998JD200032.

[26] L. Di Girolamo and R. Davies, "A band-differenced angular signature technique for cirrus cloud detection," *IEEE Trans. Geosci. Remote Sens.*, vol. 32, no. 4, pp. 890–896, Jul. 1994, doi: 10.1109/36.298017.

[27] A. A. Prasad and R. Davies, "Detecting tropical thin cirrus using multiangle imaging spectroradiometer's oblique cameras and modeled outgoing longwave radiation," *J. Geophys. Res. Atmos.*, vol. 117, no. D6, 2012, Art. no. D06208, doi: 10.1029/2011JD016798.

[28] K. D. Hutchison et al., "Automated cloud detection and classification of data collected by the visible infrared imager radiometer suite (VIIRS)," *Int. J. Remote Sens.*, vol. 26, no. 21, pp. 4681–4706, 2005, doi: 10.1080/01431160500196786.

[29] C. Cao et al., "Suomi NPP VIIRS sensor data record verification, validation, and long-term performance monitoring," *J. Geophys. Res. Atmos.*, vol. 118, no. 20, pp. 11664–11678, 2013, doi: 10.1002/2013JD020418.

[30] J. A. Barsi, K. Lee, G. Kvaran, B. L. Markham, and J. A. Pedelty, "The spectral response of the Landsat-8 operational land imager," *Remote Sens.*, vol. 6, no. 10, pp. 10232–10251, 2014, doi: 10.3390/rs61010232.

[31] M. Drusch et al., "Sentinel-2: ESA's optical high-resolution mission for GMES operational services," *Remote Sens. Environ.*, vol. 120, pp. 25–36, 2012, doi: 10.1016/j.rse.2011.11.026.

[32] K. Bessho et al., "An introduction to Himawari-8/9—Japan's new-generation geostationary meteorological satellites," *J. Meteorol. Soc. Jpn.*, vol. 94, no. 2, pp. 151–183, 2016, doi: 10.2151/jmsj.2016-009.

[33] J. Gurka and G. J. Dittberner, "The next generation GOES instruments: Status and potential impact," in *Proc. 5th Symp. Integr. Observ. Syst.*, 2001, pp. 237–241.

[34] T. J. Schmit, M. M. Gunshor, W. P. Menzel, J. J. Gurka, J. Li, and A. S. Bachmeier, "Introducing the next-generation advanced baseline imager on GOES-R," *Bull. Amer. Meteorol. Soc.*, vol. 86, no. 8, pp. 1079–1096, 2005, doi: 10.1175/BAMS-86-8-1079.

[35] T. J. Schmit, P. Griffith, M. M. Gunshor, J. M. Daniels, S. J. Goodman, and W. J. Lebair, "A closer look at the ABI on the GOES-R series," *Bull. Amer. Meteorol. Soc.*, vol. 98, no. 4, pp. 681–698, 2017, doi: 10.1175/BAMS-D-15-00230.1.

[36] J. Park, J. Bok, H. Oh, and H. Lim, "Development of radiometric calibration system for AMI," in *Proc. 14th Int. Conf. Space Oper.*, 2016, Art. no. 2325.

[37] CEOS, "Non-meteorological applications for next generation geostationary satellites study," 2016. [Online]. Available: http://ceos.org/document_management/Meetings/Plenary/30/Documents/6.1_Schroeder_NMA_Report_2016-09-05_v.2.00.pdf

[38] T. Y. Nakajima et al., "Theoretical basis of the algorithms and early phase results of the GCOM-C (Shikisai) SGLI cloud products," *Prog. Earth Planet. Sci.*, vol. 6, no. 52, pp. 1–25, 2019, doi: 10.1186/s40645-019-0295-9.

[39] H. Letu et al., "Ice cloud properties from Himawari-8/AHI next-generation geostationary satellite: Capability of the AHI to monitor the DC cloud generation process," *IEEE Trans. Geosci. Remote Sens.*, vol. 57, no. 6, pp. 3229–3239, Jun. 2019, doi: 10.1109/TGRS.2018.2882803.

[40] H. Letu et al., "A new benchmark for surface radiation products over the East Asia-Pacific region retrieved from the Himawari-8/AHI next-generation geostationary satellite," *Bull. Amer. Meteorol. Soc.*, vol. 103, no. 3, pp. E873–E888, 2022, doi: 10.1175/BAMS-D-20-0148.1.

[41] Y. Li and Y. Zhang, "Robust infrared small target detection using local steering kernel reconstruction," *Pattern Recognit.*, vol. 77, pp. 113–125, 2018, doi: 10.1016/j.patcog.2017.12.012.

[42] D. A. Morgan, "Deep convolutional neural networks for ATR from SAR imagery," in *Proc. Algorithms Synth. Aperture Radar Imagery*, 2015, vol. 9475, Art. no. 94750F.

[43] N. Kussul, M. Lavreniuk, S. Skakun, and A. Shelestov, "Deep learning classification of land cover and crop types using remote sensing data," *IEEE Geosci. Remote Sens. Lett.*, vol. 14, no. 5, pp. 778–782, May 2017, doi: 10.1109/LGRS.2017.2681128.

[44] Z. Wu, X. Chen, Y. Gao, and Y. Li, "Rapid target detection in high resolution remote sensing images usingYolo model," *Int. Arch. Photogrammetry Remote Sens. Spatial Inf. Sci.*, vol. 42, pp. 1915–1920, 2018, doi: 10.5194/isprs-archives-XLII-3-1915-2018.

[45] Y. Zhen, H. Liu, J. Li, C. Hu, and J.-S. Pan, "Remote sensing image object recognition based on convolutional neural network," in *Proc. 1st Int. Conf. Electron. Instrum. Inf. Syst.*, 2017, pp. 1–4, doi: 10.1109/EIIS.2017.8298722.

[46] W. He and N. Yokoya, "Multi-temporal sentinel-1 and-2 data fusion for optical image simulation," *ISPRS Int. J. Geo-Inf.*, vol. 7, no. 10, p. 389, 2018, doi: 10.3390/ijgi7100389.

[47] J. J. Hopfield, "Artificial neural networks," *IEEE Circuits Devices Mag.*, vol. 4, no. 5, pp. 3–10, Sep. 1988, doi: 10.1109/101.8118.

[48] A. Krizhevsky, I. Sutskever, and G. E. Hinton, "Imagenet classification with deep convolutional neural networks," *Proc. Adv. Neural Inf. Process. Syst.*, vol. 25, pp. 1097–1105, 2012.

[49] M. Mirza and S. Osindero, "Conditional generative adversarial nets," 2014. [Online]. Available: http://arxiv.org/abs/1411.1784

[50] P. Isola, J.-Y. Zhu, T. Zhou, and A. A. Efros, "Image-to-image translation with conditional adversarial networks," in *Proc. IEEE Comput. Soc. Conf. Comput. Vis. Pattern Recognit.*, 2017, pp. 1125–1134.

[51] K. Kim et al., "Nighttime reflectance generation in the visible band of satellites," *Remote Sens*, vol. 11, no. 18, 2019, Art. no. 2087, doi: 10.3390/rs11182087.

[52] Y. Kim and S. Hong, "Deep learning-generated nighttime reflectance and daytime radiance of the midwave infrared band of a geostationary satellite," *Remote Sens.*, vol. 11, no. 22, 2019, Art. no. 2713, doi: 10.3390/rs11222713.

[53] J.-H. Kim, S. Ryu, J. Jeong, D. So, H.-J. Ban, and S. Hong, "Impact of satellite sounding data on virtual visible imagery generation using conditional generative adversarial network," *IEEE J. Sel. Topics Appl. Earth Observ. Remote Sens.*, vol. 13, pp. 4532–4541, Aug. 2020, doi: 10.1109/JSTARS.2020.3013598.

[54] J.-E. Park, G. Kim, and S. Hong, "Green band generation for advanced baseline imager sensor using Pix2Pix with advanced baseline imager and advanced Himawari imager observations," *IEEE Trans. Geosci. Remote Sens.*, vol. 59, no. 8, pp. 6415–6423, Aug. 2021, doi: 10.1109/TGRS.2020.3032732.

[55] S. Ryu and S. Hong, "Hypothetical product generation of geostationary ocean color imager bands over the Yellow Sea and Bohai Sea using deep learning technique," *IEEE J. Sel. Topics Appl. Earth Observ. Remote Sens.*, vol. 14, pp. 7528–7543, Jul. 2021, doi: 10.1109/JSTARS.2021.3098781.

[56] Y. Kim and S. Hong, "Very short-term rainfall prediction using ground radar observations and conditional generative adversarial networks," *IEEE Trans. Geosci. Remote Sens.*, vol. 60, no. 4104308, pp. 1–8, Sep. 2021, Art. no. 4104308, doi: 10.1109/TGRS.2021.3108812.

[57] K. Tao and A. P. Barros, "Using fractal downscaling of satellite precipitation products for hydrometeorological applications," *J. Atmos. Ocean. Technol.*, vol. 27, no. 3, pp. 409–427, 2010, doi: 10.1175/2009JTECHA1219.1.

[58] Y.-J. Choi, H.-J. Ban, H.-J. Han, and S. Hong, "A maritime cloud-detection method using visible and near-infrared bands over the Yellow Sea and Bohai Sea," *Remote Sens.*, vol. 14, no. 3, p. 793, 2022, doi: 10.3390/rs14030793.

[59] J. Huang et al., "Susceptibility of aerosol optical thickness retrievals to thin cirrus contamination during the BASE-ASIA campaign," *J. Geophys. Res. Atmos.*, vol. 116, no. D8, 2011, Art. no. D08214, doi: 10.1029/2010JD014910.

[60] I. J. Goodfellow et al., "Generative adversarial networks," in *Proc. 27th Int. Conf. Neural Inf. Process. Syst.*, Montreal, Canada, Dec. 2014, pp. 2672–2680.

[61] A. Radford, L. Metz, and S. Chintala, "Unsupervised representation learning with deep convolutional generative adversarial networks," in *Proc. Int. Conf. Learn. Representations*, May 2016.

[62] V. Nguyen, T. F. Y. Vicente, M. Zhao, M. Hoai, and D. Samaras, "Shadow detection with conditional generative adversarial networks," in *Proc. IEEE Int. Conf. Comput. Vis.*, 2017, pp. 4510–4518.

[63] Y.-C. Lin, "Pix2Pix-tensorflow," 2017. [Online]. Available: https://github.com/yenchenlin/pix2pix-tensorflow

[64] O. Ronneberger, P. Fischer, and T. Brox, "U-net: Convolutional networks for biomedical image segmentation," in *Proc. Med. Image Comput. Comput.-Assist. Interv.*, 2015, pp. 234–241.

[65] D. P. Kingma and J. Ba, "Adam: A method for stochastic optimization," 2014, *arXiv:1412.6980*.

[66] L. Palchetti, G. Di Natale, and G. Bianchini, "Remote sensing of cirrus cloud microphysical properties using spectral measurements over the full range of their thermal emission," *J. Geophys. Res. Atmos.*, vol. 121, no. 18, pp. 10804–10819, 2016, doi: 10.1002/2016JD025162.

[67] P. Yang et al., "Radiative properties of cirrus clouds in the infrared (8–13μm) spectral region," *J. Quantitative Spectrosc. Radiative Transfer*, vol. 70, no. 4–6, pp. 473–504, 2001, doi: 10.1016/S0022-4073(01)00024-3.

[68] D. L. Mitchell, "Effective diameter in radiation transfer: General definition, applications, and limitations," *J. Atmos. Sci.*, vol. 59, no. 15, pp. 2330–2346, 2002.

[69] B. A. Baum, A. J. Heymsfield, P. Yang, and S. T. Bedka, "Bulk scattering properties for the remote sensing of ice clouds. Part I: Microphysical data and models," *J. Appl. Meteorol. Climatol.*, vol. 44, no. 12, pp. 1885–1895, 2005, doi: 10.1175/JAM2308.1.

[70] B. A. Baum et al., "Bulk scattering properties for the remote sensing of ice clouds. Part II: Narrowband models," *J. Appl. Meteorol. Climatol.*, vol. 44, no. 12, pp. 1896–1911, 2005, doi: 10.1175/JAM2309.1.

[71] A. J. Baran, "A review of the light scattering properties of cirrus," *J. Quantitative Spectrosc. Radiative Transfer*, vol. 110, no. 14–16, pp. 1239–1260, 2009, doi: 10.1016/j.jqsrt.2009.02.026.

[72] B. A. Baum, P. Yang, S. Nasiri, A. K. Heidinger, A. Heymsfield, and J. Li, "Bulk scattering properties for the remote sensing of ice clouds. Part III: High-resolution spectral models from 100 to 3250 cm− 1," *J. Appl. Meteorol. Climatol.*, vol. 46, no. 4, pp. 423–434, 2007, doi: 10.1175/JAM2473.1.

[73] T. Inoue, "On the temperature and effective emissivity determination of semi-transparent cirrus clouds by bi-spectral measurements in the 10μm window region," *J. Meteorol. Soc. Jpn.*, vol. 63, no. 1, pp. 88–99, 1985, doi: 10.2151/jmsj1965.63.1_88.

[74] A. K. Heidinger et al., "ABI cloud products from the GOES-R series," in *The GOES-R Series: A New Generation of Geostationary Environmental Satellites*, S. J. Goodman, T. J. Schmit, J. Daniels, and R. J. Redmon, Eds. Amsterdam, The Netherlands: Elsevier, 2020, pp. 43–62.

[75] I. Lensky and D. Rosenfeld, "Clouds-aerosols-precipitation satellite analysis tool (CAPSAT)," *Atmos. Chem. Phys.*, vol. 8, no. 22, pp. 6739–6753, 2008, doi: 10.5194/acp-8-6739-2008.

[76] B. Thies, T. Nauss, and J. Bendix, "First results on a process-oriented rain area classification technique using meteosat second generation SEVIRI nighttime data," *Adv. Geosci.*, vol. 16, pp. 63–72, 2008, doi: 10.5194/adgeo-16-63-2008.

[77] J. Roskovensky and K. Liou, "Detection of thin cirrus using a combination of 1.38-μm reflectance and window brightness temperature difference," *J. Geophys. Res. Atmos.*, vol. 108, no. D18, 2003, Art. no. 4570, doi: 10.1029/2002JD003346.

[78] B. Purbantoro et al., "Comparison of cloud type classification with split window algorithm based on different infrared band combinations of Himawari-8 satellite," *Adv. Remote Sens.*, vol. 7, no. 3, pp. 218–234, 2018, doi: 10.4236/ars.2018.73015.

[79] H. Shang, L. Chen, H. Letu, M. Zhao, S. Li, and S. Bao, "Development of a daytime cloud and haze detection algorithm for Himawari-8 satellite measurements over central and eastern China," *J. Geophys. Res. Atmos.*, vol. 122, no. 6, pp. 3528–3543, 2017, doi: 10.1002/2016JD025659.

[80] N. Hayatbini et al., "Conditional generative adversarial networks (cGANs) for near real-time precipitation estimation from multispectral GOES-16 satellite imageries—PERSIANN-cGAN," *Remote Sens*, vol. 11, no. 19, 2019, Art. no. 2193, doi: 10.3390/rs11192193.

[81] D. S. Wilks, "Univariate statistics," in *Statistical Methods in the Atmospheric Sciences*, D. S. Wilks, Ed. San Diego, CA, USA: Academic, 2011. pp. 21–455.

[82] N. Engerer and F. Mills, "Validating nine clear sky radiation models in Australia," *Sol. Energy*, vol. 120, pp. 9–24, 2015, doi: 10.1016/j.solener.2015.06.044.

[83] T. J. Schmit, S. S. Lindstrom, J. J. Gerth, and M. M. Gunshor, "Applications of the 16 spectral bands on the advanced baseline imager (ABI)," *J. Oper. Meteorol.*, vol. 6, no. 4, pp. 33–46, 2018, doi: 10.15191/nwajom.2018.0604.

[84] J.-M. Yeom, J.-L. Roujean, K.-S. Han, K.-S. Lee, and H.-W. Kim, "Thin cloud detection over land using background surface reflectance based on the BRDF model applied to geostationary ocean color imager (GOCI) satellite data sets," *Remote Sens. Environ.*, vol. 239, 2020, Art. no. 111610, doi: 10.1016/j.rse.2019.111610.

[85] R. A. Frey, S. A. Ackerman, R. E. Holz, S. Dutcher, and Z. Griffith, "The continuity MODIS-VIIRS cloud mask," *Remote Sens.*, vol. 12, no. 20, Art. no. 3334, 2020, doi: 10.3390/rs12203334.

[86] S. Lee and J. Choi, "Daytime cloud detection algorithm based on a multitemporal dataset for GK-2A imagery," *Remote Sens.*, vol. 13, no. 16, 2021, Art. no. 3215, doi: 10.3390/rs13163215.

[87] X. Y. Zhuge, F. Yu, and Y. Wang, "A new visible albedo normalization method: Quasi-Lambertian surface adjustment," *J. Atmos. Ocean. Technol.*, vol. 29, no. 4, pp. 589–596, 2012, doi: 10.1175/JTECH-D-11-00191.1.

Jeong-Eun Park received the B.S. degree in environmental engineering in 2019 from Sejong University, Seoul, South Korea, where she is currently working toward the integrated M.S. and Ph.D. degrees in environmental sciences.

Her research interests include remote sensing and deep learning techniques in Earth's environment.

Yun-Jeong Choi received the B.S. degree in environmental engineering from Sejong University, Seoul, South Korea, in 2020, where she is currently working toward the integrated M.S. and Ph.D. degrees in environmental sciences.

Her research interests include optical satellite remote sensing for cloud detection algorithm developments or meteorological, oceanic, and environmental satellites based on the radiative transfer model, and deep learning techniques.

Jaehoon Jeong received the Ph.D. degree in geoinformatics engineering from Inha University, Incheon, South Korea, in 2014.

He is currently a Senior Researcher with Environmental Satellite Center, National Institute of Environmental Research. His research interests include photogrammetric engineering and remote sensing data processing.

Sungwook Hong received the B.S. and M.S. degrees in earth science education from the Seoul National University, Seoul, South Korea, in 1997 and 2000, respectively, and the M.S. and Ph.D. degrees in atmospheric sciences from the Texas A&M University, College Station, TX, USA, in 2002 and 2006, respectively

From 2006 to 2008, he was a Research Scientist with the National Oceanic and Atmospheric Administration. From 2008 to 2015, he was a Senior Research Scientist with the Korea Meteorological Administration. From 2015 to 2019, he was an Assistant Professor with the Department of Environment, Energy and Geoinformatics, Sejong University, Seoul, South Korea. Since 2019, he has been an Associate Professor with the Department of Environment, Energy and Geoinformatics, Sejong University, Seoul, South Korea. He has authored more than 65 articles, and more than 20 inventions. His research interests include satellite remote sensing algorithm developments based on physical methods and artificial intelligence techniques, sensor development, and various applications in atmosphere, ocean, surface, and environment.